




Article

Coupling Plant Polyphenol Coordination Assembly with $\text{Co}(\text{OH})_2$ to Enhance Electrocatalytic Performance towards Oxygen Evolution Reaction

Xue-Zhi Song ¹ , Yu-Hang Zhao ¹, Fan Zhang ¹, Jing-Chang Ni ¹, Zhou Zhang ¹, Zhenquan Tan ¹ ,
Xiao-Feng Wang ^{2,*}  and Yanqiang Li ^{3,*}

¹ State Key Laboratory of Fine Chemicals, School of Chemical Engineering, Dalian University of Technology, Dalian 116024, China

² Key Laboratory of Materials Modification by Laser Ion and Electron Beams, Ministry of Education, School of Physics, Dalian University of Technology, Dalian 116024, China

³ School of Materials Science and Engineering, North China University of Water Resources and Electric Power, Zhengzhou 450045, China

* Correspondence: wangxf@dlut.edu.cn (X.-F.W.); lyqncwu@126.com (Y.L.)

Abstract: The oxygen evolution reaction (OER) is kinetically sluggish due to the limitation of the four-electron transfer pathway, so it is imperative to explore advanced catalysts with a superior structure and catalytic output under facile synthetic conditions. In the present work, an easily accessible strategy was proposed to implement the plant-polyphenol-involved coordination assembly on $\text{Co}(\text{OH})_2$ nanosheets. A TA-Fe (TA = tannic acid) coordination assembly growing on $\text{Co}(\text{OH})_2$ resulted in the heterostructure of $\text{Co}(\text{OH})_2$ @TA-Fe as an electrocatalyst for OER. It could significantly decrease the overpotential to 297 mV at a current density of 10 mA cm^{-2} . The heterostructure $\text{Co}(\text{OH})_2$ @TA-Fe also possessed favorable reaction kinetics with a low Tafel slope of 64.8 mV dec^{-1} and facilitated a charge-transfer ability. The enhanced electrocatalytic performance was further unraveled to be related to the confined growth of the coordination assembly on $\text{Co}(\text{OH})_2$ to expose more active sites, the modulated surface properties and their synergistic effect. This study demonstrated a simple and feasible strategy to utilize inexpensive biomass-derived substances as novel modifiers to enhance the performance of energy-conversion electrocatalysis.

Keywords: $\text{Co}(\text{OH})_2$; tannic acid; electrocatalyst; OER; coordination assembly



Citation: Song, X.-Z.; Zhao, Y.-H.; Zhang, F.; Ni, J.-C.; Zhang, Z.; Tan, Z.; Wang, X.-F.; Li, Y. Coupling Plant Polyphenol Coordination Assembly with $\text{Co}(\text{OH})_2$ to Enhance Electrocatalytic Performance towards Oxygen Evolution Reaction. *Nanomaterials* **2022**, *12*, 3972. <https://doi.org/10.3390/nano12223972>

Academic Editor: Stefano Agnoli

Received: 19 October 2022

Accepted: 6 November 2022

Published: 11 November 2022

Publisher's Note: MDPI stays neutral with regard to jurisdictional claims in published maps and institutional affiliations.



Copyright: © 2022 by the authors. Licensee MDPI, Basel, Switzerland. This article is an open access article distributed under the terms and conditions of the Creative Commons Attribution (CC BY) license (<https://creativecommons.org/licenses/by/4.0/>).

1. Introduction

The growing energy and environmental problems caused by the depletion of fossil fuels have led to a desire for clean and sustainable energy [1,2]. The oxygen evolution reaction, as one key reaction in the conversion of electrolytic water to hydrogen [3], nitrogen reduction [4] and metal–air batteries [5], is still limited by the slow four-electron process experienced at the anode [6,7]. In the search for suitable electrocatalysts to reduce the overpotential and speed up the reaction rate, Ru and Ir among the noble metals are preferred, but their high cost and low reserves have prevented us from using them on a large scale [8,9]. Therefore, researchers have turned their attention to transition-metal-based catalysts to find cheaper, better performing alternatives.

Current transition metal-based catalysts include oxides, phosphides, hydroxides, sulfides, high entropy alloys and so on [10–16]. Hydroxides have a unique structure and redox properties that provide more active sites in the OER process and alter the adsorption energy of the intermediate, thus effectively facilitating electron transport [17]. As a typical transition metal hydroxide, $\text{Co}(\text{OH})_2$ has both α and β crystalline forms, but its insufficient surface area and low inherent catalytic ability in each site limits its electrochemical performance [18]. Therefore, the design of catalysts usually starts with the preparation of

nanostructures, such as nanosheets or nanoassemblies, to increase the number of electrochemically active sites. The thickness of Co-based lamellar hydroxides has a key influence on its properties [19–21]. For example, Duraivel et al. grew layered 3D flower-like $\text{Co}(\text{OH})_2$ on nickel foam, which greatly enhanced the ion transport rate and enhanced the catalytic efficiency of electrolytic water [22]. In addition, many other approaches have been demonstrated to explore advanced hydroxide-based materials for highly efficient electrocatalysis, such as heteroatom doping and vacancy engineering [23,24]. The creation of heterointerfaces between the hydroxide substrate and functional entity is one vital blueprint to further trigger electrochemical reactions. The heterogeneous interface can synergistically expose more active sites, regulate the electronic structure to promote the intrinsic activity and even enhance the stability, comprehensively optimizing the electrocatalytic OER performance. For instance, noble metal blocks loaded on hydroxides can modulate the oxidation states of a transition metal center, tune the adsorption ability of intermedia to strengthen per-site electrocatalytic activity and even change the catalytic mechanism to interfacial direct O-O coupling, as demonstrated by Yamauchi and our group [25–27]. Moreover, metal–organic coordination units, usually researched as MOFs, have been integrated with hydroxide to heterostructures for efficient electrocatalysis due to their adjustable composition and interfacial interaction [28–30].

As one important coordination member, metal–polyphenol coordination networks have recently attracted much attention in electrocatalysis. Tannic acid, a natural polyphenol derived from plants, is inexpensive and environmentally friendly, and its numerous hydroxyl groups allow it to be assembled with a variety of metal ions [31]. Most of the substances formed by tannic acid with metal ions are amorphous and can expose more active sites, thus enhancing electrocatalytic activity [32,33]. A number of assemblies of tannic acid with metal ions have been reported, using surface engineering strategies to modify the interfacial and surface properties of non-homogeneous catalysts to significantly improve the catalytic activity of water electrolysis [34,35]. At the same time, the high affinity of tannic acid for the substrate enables the assembly of small and dispersed nanoalloy particles through the abundance of functional groups [36,37]. Therefore, it can be deemed that the assembly of one metal–polyphenol coordination unit on another hydroxide material will lead to superior electrocatalytic performance for the OER.

In this work, we developed a simple and rapid synthetic method to prepare TA-Fe complexes engineered on $\text{Co}(\text{OH})_2$, significantly decreasing the overpotential to 297 mV to achieve a current density of 10 mA cm^{-2} and possessing a small Tafel slope of 64.8 mV dec^{-1} . This easily synthesized route in an aqueous solution under an ambient environment could provide significant prospective to develop coordination-assembly-involved heterostructures for efficient OER electrocatalysis.

2. Materials and Methods

2.1. Materials

Cobalt nitrate hexahydrate ($\text{Co}(\text{NO}_3)_2 \cdot 6\text{H}_2\text{O}$), cetyltrimethylammonium bromide (CTAB), potassium hydroxide (KOH) and ferric chloride hexahydrate ($\text{FeCl}_3 \cdot 6\text{H}_2\text{O}$) were provided by Tianjin Damao Chemical Reagent corporation. Tannic acid (TA) and sodium borohydride (NaBH_4) were purchased from Aladdin. Nafion solution (5 wt%) was purchased from the Aldrich corporation. All chemicals were used directly without further purification. In addition to the above, carbon paper was purchased from the Jinglong Special Carbon Company, Beijing, China.

2.2. Synthesis of $\text{Co}(\text{OH})_2$

$\text{Co}(\text{NO}_3)_2 \cdot 6\text{H}_2\text{O}$ (2 mmol, 0.582 g) and 0.5 g of CTAB were dissolved in deionized water (25 mL) and stirred for 30 min to obtain homogeneous solution A. Then, NaBH_4 (0.1 g) was dissolved in 10 mL of deionized water to obtain solution B. The as-prepared solution B was added to solution A drop by drop. When the color of the reaction mixture had completely changed from black to green, the product of $\text{Co}(\text{OH})_2$ was collected by

centrifugation and washed three times with deionized water and ethanol. Finally, the products were placed in an oven at 60 °C for drying.

2.3. Synthesis of Co(OH)₂@TA-Fe

The as-prepared Co(OH)₂ (20 mg) sample was ultrasonically dispersed in 5 mL of deionized water. Tannic acid (81.6 mg) was dissolved in deionized water (2 mL) and 1 M KOH (160 µL) was added dropwise. A total of 200 µL of the configured tannic acid (TA) solution was added to the Co(OH)₂ suspension and stirred for 10 min, and then 7.47 mg of FeCl₃·6H₂O was added and continuously stirred for two hours. In addition, the product was finally collected by centrifugation, washed three times with deionized water and ethanol and then placed in an oven to dry. The product was denoted as Co(OH)₂@TA-Fe.

2.4. Synthesis of Co(OH)₂@TA, Co(OH)₂@Fe and TA-Fe

The preparation process of Co(OH)₂@TA-Fe was followed to prepare Co(OH)₂@TA and TA-Fe, except that FeCl₃·6H₂O or Co(OH)₂ was not present. The sample obtained under the addition of 10 µL of 1 M KOH without the addition of tannic acid was named as Co(OH)₂@Fe.

2.5. Materials Characterization

The morphological characterization was performed by field emission scanning electron microscopy (FESEM, NovaSEM 450) with an accelerating voltage of 18 kV and transmission electron microscopy (TEM, FEI Tecnai G2 F30). The crystal structure was characterized by X-ray powder diffraction (XRD, XRD-7000S), the tests were performed under Cu-Kα (λ = 1.5406 Å) radiation and the scans were performed at 5° min⁻¹ in the range of 5–80°. In addition, the surface analysis of the samples was performed by Fourier transform infrared spectroscopy (FT-IR, Nicolet iN10) and X-ray photoelectron spectroscopy (XPS, ESCALABTM 250Xi) manufactured by ThermoFisher, Waltham, MA, USA. ICP testing was conducted on a 7900X model from Agilent.

2.6. Electrochemical Measurements

All electrochemical measurements were performed at room temperature using a CHI660E workstation with a three-electrode system from C&H Instruments, Shanghai. The electrolysis cell made of quartz had a capacity of 300 mL and was equipped with a Teflon cover (Tianjin Aida Hengsheng Technology Development Co., Ltd., Tianjin, China). A glassy carbon electrode loaded with catalyst was used as the working electrode, a carbon rod as the counter electrode and Hg/HgO as the reference electrode to form the three-electrode system. A total of 1 M KOH was used as the electrolyte. Catalyst ink was obtained by ultrasonically dispersing 4 mg of catalyst in 480 µL of deionized water, 480 µL of anhydrous ethanol and 40 µL of Nafion solution. A total of 16 µL of catalyst ink was added to the glassy carbon electrode in two drops. The loading of catalyst on the glassy carbon electrode was 0.326 mg cm⁻². The data were transformed relative to a reversible hydrogen electrode (RHE) using the following Equation:

$$E_{\text{RHE}} = E_{\text{Hg}/\text{HgO}} + 0.0591 * \text{pH} + 0.098 \text{ V (pH} = 13.98) \quad (1)$$

Linear sweep voltammetry (LSV) curves were obtained at a scan rate of 5 mV s⁻¹. Cyclic voltammetry (CV) curves were obtained using different scan rates of 20–100 mV s⁻¹ at a voltage range of 0.05 to 0.15 V (vs. E_{Hg/HgO}) and the double-layer capacitance (C_{dl}) calculation was conducted. Electrochemical impedance spectroscopy (EIS) measurements were taken over a frequency range of 0.01–10⁵ Hz (AC amplitude: 5 mV) from an overpotential of 297 mV. Stability tests were performed with the catalyst (1 mg cm⁻²) loaded on carbon paper.

3. Results and Discussion

The route used to fabricate $\text{Co(OH)}_2\text{@TA-Fe}$ is shown in Figure 1a. Firstly, a dense nanosheet network structure of Co(OH)_2 was prepared by the surfactant-assisted simultaneous reduction–hydrolysis method [38]. The Co(OH)_2 material was utilized as a template to grow TA-Fe complexes on the surface, leading to the formation of $\text{Co(OH)}_2\text{@TA-Fe}$ heterostructures.

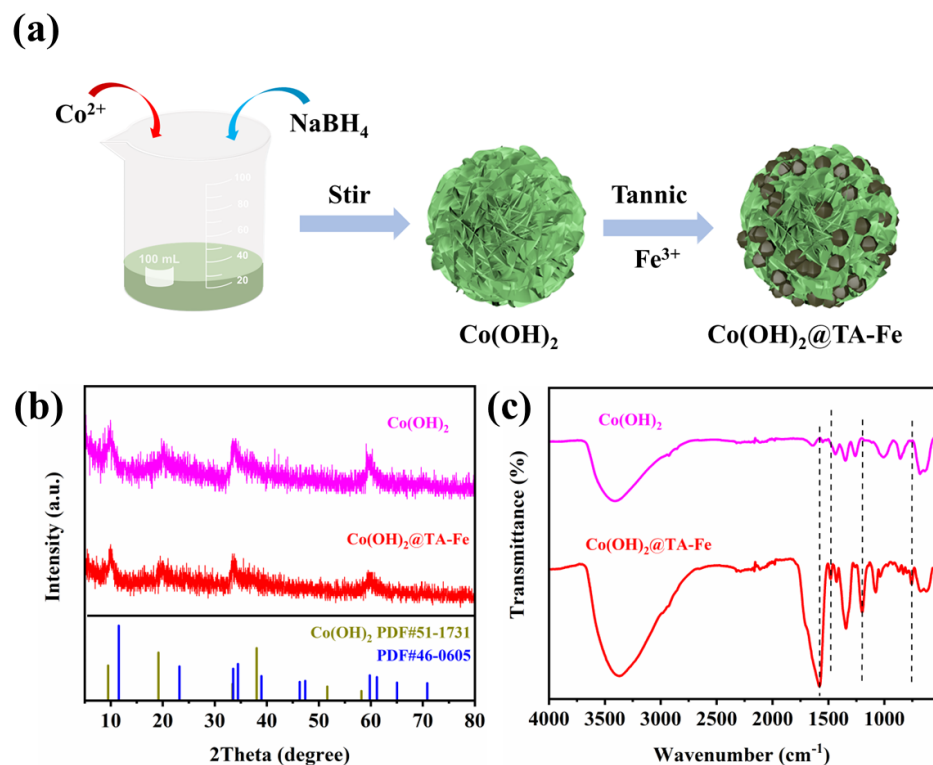


Figure 1. (a) Schematic image of the preparation route of $\text{Co(OH)}_2\text{@TA-Fe}$. (b) XRD patterns and (c) FT–IR spectra of Co(OH)_2 and $\text{Co(OH)}_2\text{@TA-Fe}$.

The crystallinity of the as-synthesized materials was confirmed by powder XRD, as shown in Figure 1b. In the PXRD pattern of pristine Co(OH)_2 , distinct diffraction peaks at two-theta values of about 9.5° and 19.1° could be indexed to the (001) and (002) crystal planes of Co(OH)_2 (JCPDS No. 51-1731), and extra diffraction peaks at 33.5° , 34.5° , 59.8° and 70.8° corresponded to the (100), (102), (110) and (202) crystalline planes, respectively (JCPDS No. 46-0605). When tannic acid was chelated with Fe^{3+} ions on the surface, the XRD pattern showed no change. This revealed that the coordinative assembly did not change the basic structure of the original Co(OH)_2 and the metal–phenol coordination compound was amorphous. [39,40]. In the FT-IR spectrum of $\text{Co(OH)}_2\text{@TA-Fe}$, the absorption peaks at 3415 , 2922 cm^{-1} were attributed to aromatic O–H stretching vibration and C–H stretching, respectively. The peaks at 1575 , 1484 and 1204 cm^{-1} belonged to aromatic C=C and phenolic C–O stretching in TA anions compared to the pure Co(OH)_2 . The successful coordinative assembling of the complex between the metallic Fe^{3+} ions and tannic acid on Co(OH)_2 could be demonstrated by the above. For comparison, samples were made without the addition of tannic acid or $\text{FeCl}_3\cdot 6\text{H}_2\text{O}$, or without the addition of Co(OH)_2 precursors, and the effect of tannic acid addition on the catalyst was also compared. After the ICP test, it was found that the Co and Fe content of the $\text{Co(OH)}_2\text{@TA-Fe}$ samples were 30.41 and 4.01% (wt%), respectively (Table S1).

The morphologies were characterized by scanning electron microscopy. As shown in Figure S1, the Co(OH)_2 was formed by a large number of cross-linking nanosheets, which could provide sufficient regions to attract exogenous components for assembly to form

heterostructures. The co-addition of tannic acid and $\text{FeCl}_3 \cdot 6\text{H}_2\text{O}$ led to the formation of a large number of metal-TA particles on the surface (Figure 2a–c). In addition, comparing $\text{Co}(\text{OH})_2@TA$ with $\text{Co}(\text{OH})_2@Fe$ together, the combination of individual tannic acid or FeCl_3 with $\text{Co}(\text{OH})_2$ did not destroy the overall nano-flake morphology of the $\text{Co}(\text{OH})_2$ (Figures S2 and S3). If the tannic acid was coordinated with $\text{FeCl}_3 \cdot 6\text{H}_2\text{O}$ directly in the absence of a $\text{Co}(\text{OH})_2$ substrate, irregular large particles were produced (Figure S4). This striking morphological difference suggested the confined growth of the coordination assembly on $\text{Co}(\text{OH})_2$. Further observation of the detailed structure of the $\text{Co}(\text{OH})_2@TA-Fe$ using transmission electron microscopy (TEM) revealed that the $\text{Co}(\text{OH})_2$ nanosheets were wrapped with many TA-Fe nanoparticles (Figure 2d,e), which was consistent with the SEM observations. There were no obvious lattice stripes on the high-resolution TEM images, demonstrating the formation of an amorphous phase of TA-Fe particles (Figure 2f). In the elemental mapping images, a uniform distribution of C, Co, Fe and O elements was observed (Figure 2g). According to the EDS elemental analysis, the weight ratios of Fe and Co were 4.1% and 24.19% (wt%), respectively, which were close to the results obtained from the ICP testing (Figure S5 and Table S2).

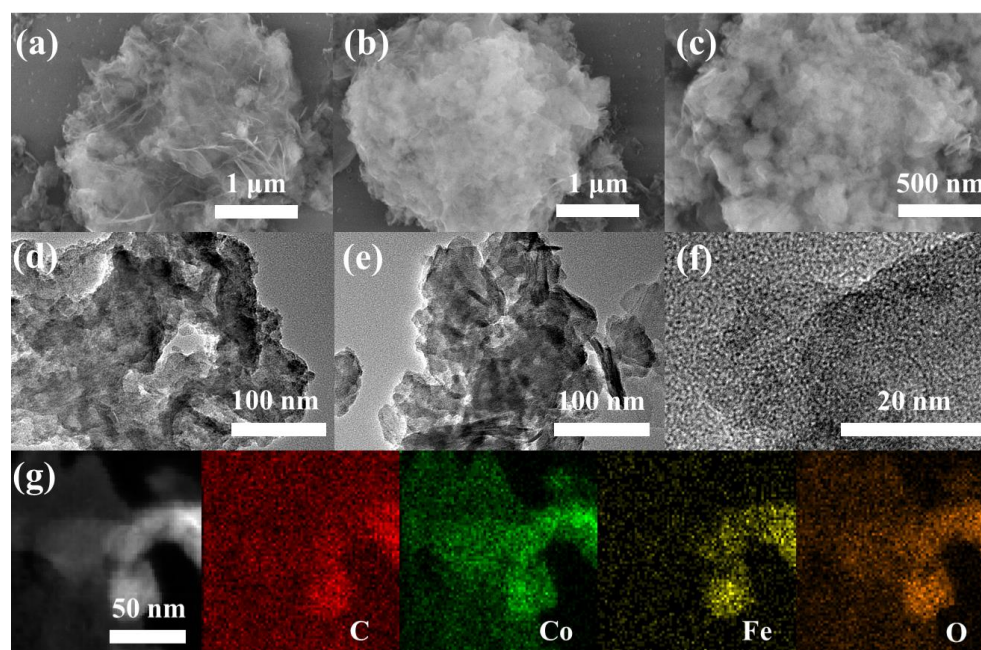


Figure 2. SEM images (a–c), TEM images (d,e), HRTEM images (f) and elemental mapping (g) of $\text{Co}(\text{OH})_2@TA-Fe$.

The elemental chemical bonding states of the $\text{Co}(\text{OH})_2@TA-Fe$ were investigated by X-ray photoelectron spectroscopy (Figure S6). Figure 3a shows the XPS spectra of element C. The binding energy peaks at 284.5, 286.2 and 288.4 eV belonged to C–C, C–O and C=O [41], respectively, while in the XPS spectrum of O, the binding energy located at 530.4 eV was attributed to metal–O bonding, and 531.3, 532.3 and 533.2 eV were attributed to C=O, O–H and C–O, respectively [42,43]. The XPS spectra of Fe showed that 711.2, 714.8 and 724.1 eV belonged to Fe^{3+} and 719.1 eV was the satellite peak of Fe^{3+} (Figure 3c) [44,45]. Finally, the XPS of Co was split into 781.1 and 796.9 eV attributed to Co^{2+} and 785.8 and 802.6 eV attributed to their satellite peaks, which were not quite different from the XPS of the $\text{Co}(\text{OH})_2$ (Figure S7) [46]. The above analyses further proved the formation of the TA-Fe complex and its successful attachment on $\text{Co}(\text{OH})_2$. The weight of Fe and Co for the $\text{Co}(\text{OH})_2@TA-Fe$ obtained by XPS calculations were 13.9% and 26.36% (wt%) (Table S3). The large difference in the contents determined by XPS and other methods may be due to the structure that the TA-Fe loaded on the $\text{Co}(\text{OH})_2$ surface. Therefore, the amount of iron

determined on the surface was larger than that determined by other methods, since XPS is a surface-sensitive analytical method.

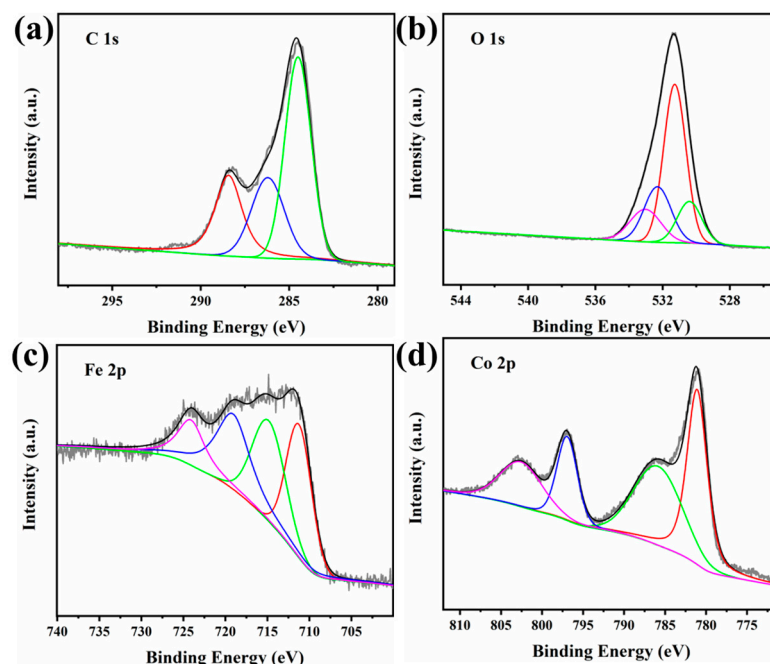


Figure 3. XPS spectra of $\text{Co(OH)}_2@TA\text{-Fe}$: C 1s (a), O 1s (b), Fe 2p (c) and Co 2p (d).

The catalysts were tested for their OER electrocatalytic performance using the assembled three-electrode system in 1 M KOH solution. As shown in Figure 4a, the linear sweep voltammetry curves of all samples were not iR compensated. The overpotential of the $\text{Co(OH)}_2@TA\text{-Fe}$ sample was 297 mV with respect to the reference current density of 10 mA cm^{-2} . This overpotential of 297 mV was much lower than that of the $\text{Co(OH)}_2@TA$ (361 mV), $\text{Co(OH)}_2@Fe$ (381 mV), TA-Fe (427 mV) and Co(OH)_2 (455 mV). This demonstrated that compounding TA-Fe particles with Co(OH)_2 substantially improved the electrocatalytic activity of the catalysts. The overpotential of the $\text{Co(OH)}_2@TA\text{-Fe}$ increased when the amount of feeding tannic acid increased (Figure S8), proving that the formation of more TA-Fe complexes did not lead to further performance enhancement of the samples. Samples with different feeding Fe amounts were also prepared, and it was again proved that $\text{Co(OH)}_2@TA\text{-Fe}$ with a proper amount of source Fe possessed excellent electrocatalytic properties (Figure S9). Moreover, the Tafel slope of the $\text{Co(OH)}_2@TA\text{-Fe}$ (64.8 mV dec^{-1}) was lower than that of the $\text{Co(OH)}_2@TA$ (75.9 mV dec^{-1}), $\text{Co(OH)}_2@Fe$ (79.2 mV dec^{-1}), TA-Fe (66.1 mV dec^{-1}) and Co(OH)_2 ($133.3 \text{ mV dec}^{-1}$), suggesting its faster intrinsic reaction kinetics enabled by the $\text{Co(OH)}_2@TA\text{-Fe}$ heterostructure. Compared with many recently reported catalysts (Table S4), such as $\text{Co}_{3-x}\text{Fe}_x\text{O}_4$ (294 mV, 47.3 mV dec^{-1}) [47], $\text{MPN@Fe}_3\text{O}_4$ (260 mV, 33.6 mV dec^{-1}) [48], $\text{CoFe(OH)}_x/\text{GO}$ (294 mV, 63.1 mV dec^{-1}) [49], $\text{TF@Co(OH)}_2\text{-500}$ (317 mV, 47 mV dec^{-1}) [50] and $\text{CeO}_2@\text{Co(OH)}_2$ (310 mV, 66 mV dec^{-1}) [51], the $\text{Co(OH)}_2@TA\text{-Fe}$ had a comparable or even better catalytic performance.

To further disclose the inherent reason for the impressive electrocatalytic activity, the electrochemical surface area (ECSA) of the electrocatalyst was estimated by electrochemical double-layer capacitance (C_{dl}) using cyclic voltammetry (CV) in the non-Faraday current region at different scan rates (Figure S10). As shown in Figure 4c, the C_{dl} values for the $\text{Co(OH)}_2@TA\text{-Fe}$ (0.53 mF cm^{-2}) were larger than those for the $\text{Co(OH)}_2@Fe$ (0.13 mF cm^{-2}) and TA-Fe (0.09 mF cm^{-2}), but smaller than those for the $\text{Co(OH)}_2@TA$ (1.59 mF cm^{-2}) and Co(OH)_2 (0.74 mF cm^{-2}). ECSA values can be obtained from C_{dl} , which can help to understand the effect between surface roughness in terms of morphology and improvement in terms of catalytic performance. At reaching an ECSA-normalized current density of 1 mA cm^{-2} (Figure 4d), the $\text{Co(OH)}_2@TA\text{-Fe}$ only required 1.534 V compared to the $\text{Co(OH)}_2@TA$

(1.692 V), $\text{Co(OH)}_2@Fe$ (1.565 V) and TA-Fe (1.617 V). These compared results implied that the heterostructure with a coordination assembly on the Co(OH)_2 could enhance the intrinsic per-site activity towards the OER. In addition, the EIS values of the different samples were measured to further characterize the charge-transfer ability at the electrode/electrolyte interface during OER catalysis. As shown in the Nyquist plot (Figure 4e), the $\text{Co(OH)}_2@TA$ -Fe catalyst had the smallest radius among these five electrocatalysts and exhibited the smallest charge-transfer resistance, demonstrating that combining TA-Fe with Co(OH)_2 could effectively reduce the charge-transfer impedance and enhance the OER activity by increasing the charge-transfer rate. Long-term stability is another important factor in judging the performance of a catalyst. As shown in Figure 4f, after continuously applying a bias for 24 h, the current density of the $\text{Co(OH)}_2@TA$ -Fe catalyst showed almost a straight line with negligible attenuation, further demonstrating its excellent electrochemical stability.

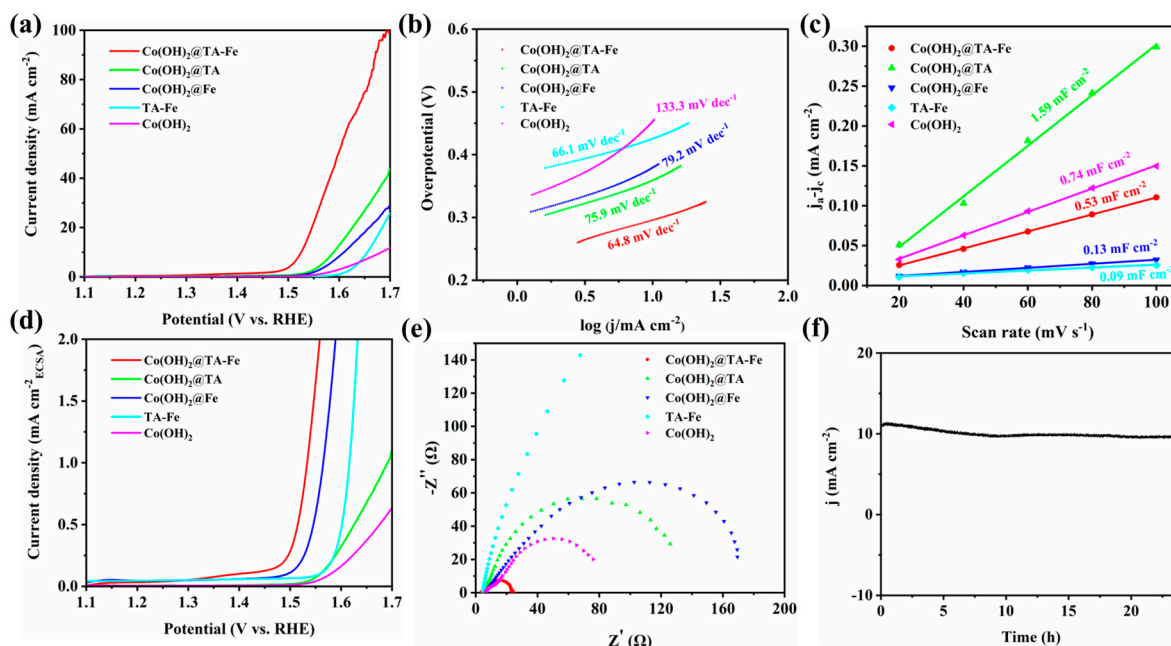


Figure 4. (a) LSV curves, (b) Tafel slopes, (c) C_{dl} calculations, (d) LSV curve normalized by ECSA and (e) Nyquist plots for $\text{Co(OH)}_2@TA$ -Fe, $\text{Co(OH)}_2@Fe$, TA-Fe, $\text{Co(OH)}_2@TA$ and Co(OH)_2 . (f) Long-term stability of $\text{Co(OH)}_2@TA$ -Fe.

In the SEM image of the $\text{Co(OH)}_2@TA$ -Fe sample after the stability test (Figure 5a,b), no obvious nanosheet structure could be observed. In contrast, there were agglomerated bulk particles. The corresponding XPS analysis was also performed. The Co 2p 3/2 peak showed a negative shift from 781.1 to 779.9 eV, indicating a conversion from Co^{2+} to Co^{3+} after OER catalysis (Figure 5c) [52]. Satellite peaks at 707.2 eV attributed to Fe^0 and 733.5 eV attributed to Fe^{2+} were also observed (Figure 5d) [53,54]. The presence of Fe^0 could increase the conductivity and promote the appearance of CoOOH material that is favorable to OER [55]. In addition, the metal phenolic network formed by the tannic acid and Fe could prevent the loss of Fe and further enhance the stability of the catalyst. Therefore, its excellent OER performance allows $\text{Co(OH)}_2@TA$ -Fe to be a promising anodic candidate for water electrolysis.

In combination with the above experimental analysis, the enhanced electrocatalytic performance of the Co(OH)_2 modified by the complexation of tannic acid with iron could be attributed to the following points: (i) Co(OH)_2 nanosheets could be used as a substrate with a large specific surface area to shorten the ion and electron diffusion pathways; (ii) using Co(OH)_2 as a substrate could prevent the tannic acid from complexing with metal ions in large quantities to form bulk particles, which could expose more active sites; (iii) water molecules

are more favorable to adsorb on Fe^{3+} than Co^{2+} [56], and the TA-Fe could change the surface properties of the catalyst; and v) this synergistic effect of heterogeneous structure.

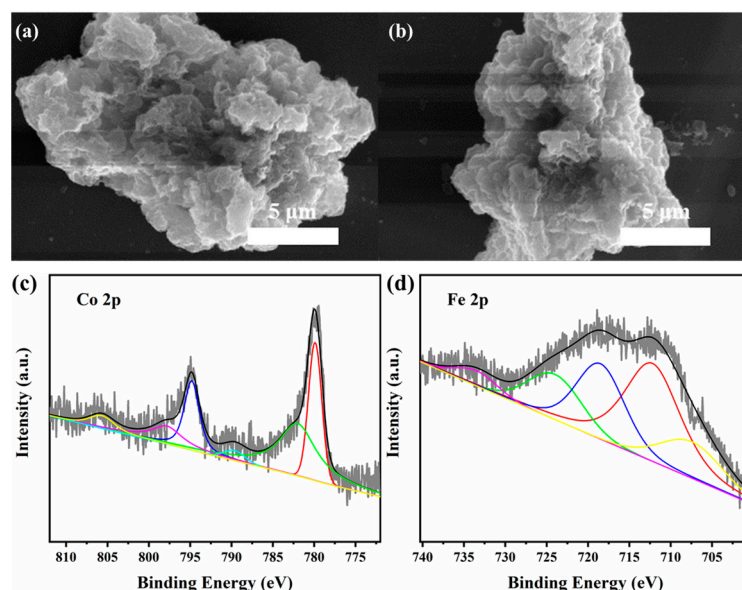


Figure 5. (a,b) SEM images of $\text{Co(OH)}_2@TA\text{-Fe}$ that had undergone stability test and XPS spectra of $\text{Co(OH)}_2@TA\text{-Fe}$ after stability test: (c) Co 2p region, (d) Fe 2p region.

4. Conclusions

In summary, $\text{Co(OH)}_2@TA\text{-Fe}$ catalysts were successfully demonstrated by rational surface engineering with TA-Fe coordination units on the surface of Co(OH)_2 nanosheets. The confined growth of exogenous assemblies with amorphous features provided more active sites and simultaneously enriched the interfaces. The heterostructured coordination assembly could significantly enhance the electrocatalytic activity with only 297 mV of $\text{Co(OH)}_2@TA\text{-Fe}$ required to reach 10 mA cm^{-2} . Moreover, it also induced more favorable reaction kinetics and improved the charge-transfer ability and intrinsic activity of the catalytic site. This work can open the way for fabricating multi-phase environmentally friendly and cheap catalysts towards energy conversion, in which the size, crystallinity and metal type of the metal–polyphenol entity may be designed to enhance the performance.

Supplementary Materials: The following are available online at <https://www.mdpi.com/article/10.3390/nano12223972/s1>, Figure S1: SEM images of Co(OH)_2 ; Figure S2: SEM images of $\text{Co(OH)}_2@TA$; Figure S3: SEM images of $\text{Co(OH)}_2@Fe$; Figure S4: SEM images of TA-Fe; Figure S5. EDS analysis graph of $\text{Co(OH)}_2@TA\text{-Fe}$. Figure S6: Full XPS spectrum of $\text{Co(OH)}_2@TA\text{-Fe}$; Figure S7: XPS spectra of Co(OH)_2 ; Figure S8: LSV curves for $\text{Co(OH)}_2@TA\text{-Fe}$ with different amounts of tannic acid added; Figure S9. Comparison of LSV performance tests with different Fe additions. Figure S10: CV curves of different samples; Table S1. ICP test results of $\text{Co(OH)}_2@TA\text{-Fe}$. Table S2. Results of EDS elemental analysis of $\text{Co(OH)}_2@TA\text{-Fe}$. Table S3. Surface composition of the $\text{Co(OH)}_2@TA\text{-Fe}$ obtained by XPS measurements. Table S4: Comparison of electrocatalytic performance with other catalysts. References [29,48–51,57–63] are cited in the Supplement Material.

Author Contributions: Conceptualization, Y.L., X.-Z.S. and Y.-H.Z.; methodology, X.-Z.S. and Y.-H.Z.; investigation, Y.-H.Z.; data curation, Y.-H.Z., J.-C.N., F.Z. and Z.Z.; writing—original draft preparation, Y.-H.Z.; writing—review and editing, Y.L., X.-F.W., X.-Z.S. and Z.T.; visualization, Z.T., X.-F.W. and Y.L.; funding acquisition, X.-Z.S. and X.-F.W. All authors have read and agreed to the published version of the manuscript.

Funding: This research was funded by the National Natural Science Foundation of China (grants No. 22271036), the Fundamental Research Funds for the Central Universities of China (DUT22LK15) and the Open Funds of the State Key Laboratory of Rare Earth Resource Utilization (RERU2022011).

Data Availability Statement: Not applicable.

Acknowledgments: The authors acknowledge the facilities and the scientific and technical assistance of the Instrumental Analysis & Research Center, Dalian University and the financial support from the above funding.

Conflicts of Interest: The authors declare no conflict of interest.

References

1. Kim, H.J.; Kim, H.Y.; Joo, J.; Joo, S.H.; Lim, J.S.; Lee, J.; Huang, H.; Shao, M.; Hu, J.; Kim, J.Y.; et al. Recent advances in non-precious group metal-based catalysts for water electrolysis and beyond. *J. Mater. Chem. A* **2022**, *10*, 50–88. [\[CrossRef\]](#)
2. Tang, T.; Ding, L.; Yao, Z.C.; Pan, H.R.; Hu, J.S.; Wan, L.J. Synergistic Electrocatalysts for Alkaline Hydrogen Oxidation and Evolution Reactions. *Adv. Funct. Mater.* **2021**, *32*, 2107479. [\[CrossRef\]](#)
3. Yu, M.; Budiyanto, E.; Tuysuz, H. Principles of Water Electrolysis and Recent Progress in Cobalt-, Nickel-, and Iron-Based Oxides for the Oxygen Evolution Reaction. *Angew. Chem. Int. Ed. Engl.* **2022**, *61*, e202103824. [\[PubMed\]](#)
4. Tavella, F.; Giusi, D.; Ampelli, C. Nitrogen reduction reaction to ammonia at ambient conditions: A short review analysis of the critical factors limiting electrocatalytic performance. *Curr. Opin. Green Sustain. Chem.* **2022**, *35*, 100604. [\[CrossRef\]](#)
5. Tang, W.; Li, B.; Teng, K.; Wang, X.; Liu, R.; Wu, M.; Zhang, L.; Ren, P.; Zhang, J.; Feng, M. Advanced noble-metal-free bifunctional electrocatalysts for metal-air batteries. *J. Mater.* **2022**, *8*, 454–474. [\[CrossRef\]](#)
6. Gao, L.; Cui, X.; Sewell, C.D.; Li, J.; Lin, Z. Recent advances in activating surface reconstruction for the high-efficiency oxygen evolution reaction. *Chem. Soc. Rev.* **2021**, *50*, 8428–8469. [\[CrossRef\]](#)
7. Singh, B.; Yadav, A.; Indra, A. Realizing electrochemical transformation of a metal–organic framework precatalyst into a metal hydroxide–oxy(hydroxide) active catalyst during alkaline water oxidation. *J. Mater. Chem. A* **2022**, *10*, 3843–3868. [\[CrossRef\]](#)
8. Ma, Z.; Zhang, Y.; Liu, S.; Xu, W.; Wu, L.; Hsieh, Y.-C.; Liu, P.; Zhu, Y.; Sasaki, K.; Renner, J.N.; et al. Reaction mechanism for oxygen evolution on RuO₂, IrO₂, and RuO₂@IrO₂ core-shell nanocatalysts. *J. Electroanal. Chem.* **2018**, *819*, 296–305. [\[CrossRef\]](#)
9. Escalera-López, D.; Czióska, S.; Geppert, J.; Boubnov, A.; Röse, P.; Saraçi, E.; Krewer, U.; Grunwaldt, J.-D.; Cherevko, S. Phase- and Surface Composition-Dependent Electrochemical Stability of Ir-Ru Nanoparticles during Oxygen Evolution Reaction. *ACS Catal.* **2021**, *11*, 9300–9316. [\[CrossRef\]](#)
10. Zheng, L.; Hu, L.; Hu, Y.; Liu, F.; Liu, Z.; Xue, Y.; Zhang, J.; Liu, H.; Tang, C. Interfacial modification of Co(OH)₂/Co₃O₄ nanosheet heterostructure arrays for the efficient oxygen evolution reaction. *Catal. Sci. Technol.* **2021**, *11*, 3706–3714. [\[CrossRef\]](#)
11. Vijayakumar, E.; Ramakrishnan, S.; Sathiskumar, C.; Yoo, D.J.; Balamurugan, J.; Noh, H.S.; Kwon, D.; Kim, Y.H.; Lee, H. MOF-derived CoP-nitrogen-doped carbon@NiFeP nanoflakes as an efficient and durable electrocatalyst with multiple catalytically active sites for OER, HER, ORR and rechargeable zinc-air batteries. *Chem. Eng. J.* **2022**, *428*, 131115. [\[CrossRef\]](#)
12. Yao, N.; Wang, G.; Jia, H.; Yin, J.; Cong, H.; Chen, S.; Luo, W. Intermolecular Energy Gap-Induced Formation of High-Valent Cobalt Species in CoOOH Surface Layer on Cobalt Sulfides for Efficient Water Oxidation. *Angew. Chem. Int. Ed. Engl.* **2022**, *61*, e202117178. [\[CrossRef\]](#)
13. Park, H.; Bae, J.W.; Lee, T.H.; Park, I.J.; Kim, C.; Lee, M.G.; Lee, S.A.; Yang, J.W.; Choi, M.J.; Hong, S.H.; et al. Surface-Tailored Medium Entropy Alloys as Radically Low Overpotential Oxygen Evolution Electrocatalysts. *Small* **2022**, *18*, e2105611. [\[CrossRef\]](#) [\[PubMed\]](#)
14. Wang, J.; Chen, C.; Cai, N.; Wang, M.; Li, H.; Yu, F. High topological tri-metal phosphide of CoP@FeNiP toward enhanced activities in oxygen evolution reaction. *Nanoscale* **2021**, *13*, 1354–1363. [\[CrossRef\]](#) [\[PubMed\]](#)
15. Huang, K.; Peng, D.; Yao, Z.; Xia, J.; Zhang, B.; Liu, H.; Chen, Z.; Wu, F.; Wu, J.; Huang, Y. Cathodic plasma driven self-assembly of HEAs dendrites by pure single FCC FeCoNiMnCu nanoparticles as high efficient electrocatalysts for OER. *Chem. Eng. J.* **2021**, *425*, 131533. [\[CrossRef\]](#)
16. Peng, Y.; Zhang, F.; Zhang, Y.; Luo, X.; Chen, L.; Shi, Y. N,S-Doped hollow carbon nanosheet-encapsulated Co₉S₈ nanoparticles as a highly efficient bifunctional electrocatalyst for rechargeable zinc-air batteries. *Dalton Trans* **2022**, *51*, 12630–12640. [\[CrossRef\]](#)
17. Zhang, Y.-C.; Han, C.; Gao, J.; Pan, L.; Wu, J.; Zhu, X.-D.; Zou, J.-J. NiCo-Based Electrocatalysts for the Alkaline Oxygen Evolution Reaction: A Review. *ACS Catal.* **2021**, *11*, 12485–12509. [\[CrossRef\]](#)
18. Martinez, E.Y.; Zhu, K.; Li, C.W. Influence of the Defect Stability on n-Type Conductivity in Electron-Doped alpha- and beta-Co(OH)₂ Nanosheets. *Inorg. Chem.* **2021**, *60*, 6950–6956. [\[CrossRef\]](#)
19. Huang, C.; Zhong, Y.; Chen, J.; Li, J.; Zhang, W.; Zhou, J.; Zhang, Y.; Yu, L.; Yu, Y. Fe induced nanostructure reorganization and electronic structure modulation over CoNi (oxy)hydroxide nanorod arrays for boosting oxygen evolution reaction. *Chem. Eng. J.* **2021**, *403*, 126304. [\[CrossRef\]](#)
20. McAteer, D.; Godwin, I.J.; Ling, Z.; Harvey, A.; He, L.; Boland, C.S.; Vega-Mayoral, V.; Szydłowska, B.; Rovetta, A.A.; Backes, C.; et al. Liquid Exfoliated Co(OH)₂ Nanosheets as Low-Cost, Yet High-Performance, Catalysts for the Oxygen Evolution Reaction. *Adv. Energy Mater.* **2018**, *8*, 1702965. [\[CrossRef\]](#)
21. Gu, L.-F.; Li, C.-F.; Zhao, J.-W.; Xie, L.-J.; Wu, J.-Q.; Ren, Q.; Li, G.-R. Dual modulation of lattice strain and charge polarization induced by Co(OH)₂/Ni(OH)₂ interfaces for efficient oxygen evolution catalysis. *J. Mater. Chem. A* **2021**, *9*, 13279–13287. [\[CrossRef\]](#)

22. Duraivel, M.; Nagappan, S.; Park, K.H.; Prabakar, K. Hierarchical 3D flower like cobalt hydroxide as an efficient bifunctional electrocatalyst for water splitting. *Electrochim. Acta* **2022**, *411*, 140071. [[CrossRef](#)]
23. Wang, P.; Zhang, L.; Wang, Z.; Bu, D.; Zhan, K.; Yan, Y.; Yang, J.; Zhao, B. N and Mn dual-doped cactus-like cobalt oxide nanoarchitecture derived from cobalt carbonate hydroxide as efficient electrocatalysts for oxygen evolution reactions. *J. Colloid Interface Sci.* **2021**, *597*, 361–369. [[CrossRef](#)]
24. Du, X.; Guo, J.; Chen, M.; Cheong, W.-C.; Chen, Y.; Liu, D.; Chen, S.; Wang, X.; Lo, K.H.; Hu, J.-S.; et al. Surface reconstruction on silver nanoparticles decorated trimetallic hydroxide nanosheets to generate highly active oxygen-deficient (oxy)hydroxide layer for high-efficient water oxidation. *Chem. Eng. J.* **2021**, *425*, 131662. [[CrossRef](#)]
25. Song, X.-Z.; Zhang, N.; Liu, F.; Wang, Z.-H.; Zhu, W.-Y.; Zhang, G.-Z.; Niu, Z.-Y.; Wang, X.-F.; Tan, Z. Spontaneously engineering heterogeneous interface of silver nanoparticles on α -Co(OH)₂ for boosting electrochemical oxygen evolution. *J. Alloy. Compd.* **2021**, *873*, 159766. [[CrossRef](#)]
26. Zhang, T.; Meng, Y.L.; Zhao, Y.H.; Ni, J.C.; Pan, Y.; Dai, Y.; Tan, Z.; Wang, X.F.; Song, X.Z. Boosting the oxygen evolution electrocatalysis of high-entropy hydroxides by high-valence nickel species regulation. *Chem. Commun.* **2022**, *58*, 7682–7685. [[CrossRef](#)]
27. Kitano, S.; Noguchi, T.G.; Nishihara, M.; Kamitani, K.; Sugiyama, T.; Yoshioka, S.; Miwa, T.; Yoshizawa, K.; Staykov, A.; Yamauchi, M. Heterointerface Created on Au-Cluster-Loaded Unilamellar Hydroxide Electrocatalysts as a Highly Active Site for the Oxygen Evolution Reaction. *Adv. Mater.* **2022**, *34*, e2110552. [[CrossRef](#)]
28. Song, X.Z.; Zhang, N.; Wang, X.F.; Tan, Z. Recent advances of metal-organic frameworks and their composites toward oxygen evolution electrocatalysis. *Mater. Today Energy* **2021**, *19*, 100597. [[CrossRef](#)]
29. Gong, C.; Li, W.; Lei, Y.; He, X.; Chen, H.; Du, X.; Fang, W.; Wang, D.; Zhao, L. Interfacial engineering of ZIF-67 derived CoSe/Co(OH)₂ catalysts for efficient overall water splitting. *Compos. Part B Eng.* **2022**, *236*, 109823. [[CrossRef](#)]
30. Devi, B.; Koner, R.R.; Kurungot, S. Recent advances in the metal-organic framework-based electrocatalysts for trifunctional electrocatalysis. *Dalton Trans.* **2022**, *51*, 13573–13590. [[CrossRef](#)]
31. Chen, C.; Yang, H.; Yang, X.; Ma, Q. Tannic acid: A crosslinker leading to versatile functional polymeric networks: A review. *RSC Adv.* **2022**, *12*, 7689–7711. [[CrossRef](#)] [[PubMed](#)]
32. Wang, S.; Jang, H.; Wang, J.; Wu, Z.; Liu, X.; Cho, J. Cobalt-Tannin-Framework-Derived Amorphous Co-P/Co-N-C on N, P Co-Doped Porous Carbon with Abundant Active Moieties for Efficient Oxygen Reactions and Water Splitting. *ChemSusChem* **2019**, *12*, 830–838. [[CrossRef](#)]
33. Chen, M.; Zhang, Z.; Zeng, C.; Jiang, J.; Gao, H.; Ai, L. Synergistically boosting oxygen evolution performance of iron-tannic electrocatalyst via localized photothermal effect. *Colloids Surf. A Physicochem. Eng. Asp.* **2022**, *638*, 128248. [[CrossRef](#)]
34. Wang, Y.; Chen, S.; Zhao, S.; Chen, Q.; Zhang, J. Interfacial coordination assembly of tannic acid with metal ions on three-dimensional nickel hydroxide nanowalls for efficient water splitting. *J. Mater. Chem. A* **2020**, *8*, 15845–15852. [[CrossRef](#)]
35. Wang, T.; Cao, X.; Jiao, L. MOFs-Derived Carbon-Based Metal Catalysts for Energy-Related Electrocatalysis. *Small* **2021**, *17*, e2004398. [[CrossRef](#)] [[PubMed](#)]
36. Zhao, M.; Li, H.; Yuan, W.; Li, C.M. Tannic Acid-Mediated In Situ Controlled Assembly of NiFe Alloy Nanoparticles on Pristine Graphene as a Superior Oxygen Evolution Catalyst. *ACS Appl. Energy Mater.* **2020**, *3*, 3966–3977. [[CrossRef](#)]
37. Li, H.; Shu, X.; Tong, P.; Zhang, J.; An, P.; Lv, Z.; Tian, H.; Zhang, J.; Xia, H. Fe-Ni Alloy Nanoclusters Anchored on Carbon Aerogels as High-Efficiency Oxygen Electrocatalysts in Rechargeable Zn-Air Batteries. *Small* **2021**, *17*, e2102002. [[CrossRef](#)]
38. Song, X.Z.; Zhu, W.Y.; Ni, J.C.; Zhao, Y.H.; Zhang, T.; Tan, Z.; Liu, L.Z.; Wang, X.F. Boosting Hydrogen Evolution Electrocatalysis via Regulating the Electronic Structure in a Crystalline-Amorphous CoP/CeO_x p-n Heterojunction. *ACS Appl. Mater. Interfaces* **2022**, *14*, 33151–33160. [[CrossRef](#)]
39. Fang, H.; Chen, G.; Wang, L.; Yan, J.; Zhang, L.; Gao, K.; Zhang, Y.; Wang, L. Facile fabrication of hierarchical film composed of Co(OH)₂@Carbon nanotube core/sheath nanocables and its capacitive performance. *RSC Adv.* **2018**, *8*, 38550–38555. [[CrossRef](#)]
40. Chen, L.; Zhang, H.; Chen, L.; Wei, X.; Shi, J.; He, M. Facile synthesis of Cu doped cobalt hydroxide (Cu-Co(OH)₂) nano-sheets for efficient electrocatalytic oxygen evolution. *J. Mater. Chem. A* **2017**, *5*, 22568–22575. [[CrossRef](#)]
41. Xu, Q.; Jiu, H.; Zhang, L.; Song, W.; Wei, H.; Wang, C.; Yang, J.; Guo, F.; Gao, T. Structure design of CuO/Cu₂O@C heterostructure polyhedron accumulated by hollow microspheres for high-performance lithium storage. *J. Alloy. Compd.* **2021**, *887*, 161417. [[CrossRef](#)]
42. Deng, G.; Wang, T.; Alshehri, A.A.; Alzahrani, K.A.; Wang, Y.; Ye, H.; Luo, Y.; Sun, X. Improving the electrocatalytic N₂ reduction activity of Pd nanoparticles through surface modification. *J. Mater. Chem. A* **2019**, *7*, 21674–21677. [[CrossRef](#)]
43. Shi, Y.; Yu, Y.; Liang, Y.; Du, Y.; Zhang, B. In Situ Electrochemical Conversion of an Ultrathin Tannin Nickel Iron Complex Film as an Efficient Oxygen Evolution Reaction Electrocatalyst. *Angew. Chem. Int. Ed.* **2019**, *58*, 3769–3773. [[CrossRef](#)] [[PubMed](#)]
44. Guo, D.; Han, S.; Wang, J.; Zhu, Y. MIL-100-Fe derived N-doped Fe/Fe₃C@C electrocatalysts for efficient oxygen reduction reaction. *Appl. Surf. Sci.* **2018**, *434*, 1266–1273. [[CrossRef](#)]
45. Chen, T.; Wu, J.; Zhu, C.; Liu, Z.; Zhou, W.; Zhu, C.; Guan, C.; Fang, G. Rational design of iron single atom anchored on nitrogen doped carbon as a high-performance electrocatalyst for all-solid-state flexible zinc-air batteries. *Chem. Eng. J.* **2021**, *405*, 125956. [[CrossRef](#)]
46. Peng, H.; Zhou, K.; Jin, Y.; Zhang, Q.; Liu, J.; Wang, H. Hierarchical nanostructure with ultrafine MoO₃ particles-decorated Co(OH)₂ nanosheet array on Ag nanowires for promoted hydrogen evolution reaction. *Chem. Eng. J.* **2022**, *429*, 132477. [[CrossRef](#)]

47. Xu, Z.; Zuo, W.; Shi, T.; Liu, X.; Li, H.; Zhao, P.; Cheng, G. An Fe-doped Co-oxide electrocatalyst synthesized through a post-modification method toward advanced water oxidation. *Dalton Trans.* **2022**, *51*, 3137–3145. [[CrossRef](#)]
48. Jia, X.; Wu, J.; Lu, K.; Li, Y.; Qiao, X.; Kaelin, J.; Lu, S.; Cheng, Y.; Wu, X.; Qin, W. Organic–inorganic hybrids of Fe–Co polyphenolic network wrapped Fe₃O₄ nanocatalysts for significantly enhanced oxygen evolution. *J. Mater. Chem. A* **2019**, *7*, 14302–14308. [[CrossRef](#)]
49. Cheng, J.; Yue, X.; Chen, C.; Shen, X.; Zeng, S.; Ji, Z.; Yuan, A.; Zhu, G. Template-assisted synthesis of accordion-like CoFe(OH) nanosheet clusters on GO sheets for electrocatalytic water oxidation. *J. Electroanal. Chem.* **2022**, *905*, 115957. [[CrossRef](#)]
50. Zhou, Y.N.; Fan, R.Y.; Cao, Y.N.; Wang, H.Y.; Dong, B.; Zhao, H.Y.; Wang, F.L.; Yu, J.F.; Chai, Y.M. Oriented and robust anchoring of Fe via anodic interfacial coordination assembly on ultrathin Co hydroxides for efficient water oxidation. *Nanoscale* **2021**, *13*, 13463–13472. [[CrossRef](#)]
51. Sung, M.-C.; Lee, G.-H.; Kim, D.-W. CeO₂/Co(OH)₂ hybrid electrocatalysts for efficient hydrogen and oxygen evolution reaction. *J. Alloys Compd.* **2019**, *800*, 450–455. [[CrossRef](#)]
52. Ge, R.; Ren, X.; Ji, X.; Liu, Z.; Du, G.; Asiri, A.M.; Sun, X.; Chen, L. Benzoate Anion-Intercalated Layered Cobalt Hydroxide Nanoarray: An Efficient Electrocatalyst for the Oxygen Evolution Reaction. *ChemSusChem* **2017**, *10*, 4004–4008. [[CrossRef](#)] [[PubMed](#)]
53. Lv, X.; Peng, H.; Wang, X.; Hu, L.; Peng, M.; Liu, Z.; Jiang, G. Nitrate reduction by nanoscale zero valent iron (nFe⁰)-based Systems: Mechanism, reaction pathway and strategy for enhanced N₂ formation. *Chem. Eng. J.* **2022**, *430*, 133133. [[CrossRef](#)]
54. Jin, C.; Hou, M.; Li, X.; Liu, D.; Qu, D.; Dong, Y.; Xie, Z.; Zhang, C. Rapid electrodeposition of Fe-doped nickel selenides on Ni foam as a bi-functional electrocatalyst for water splitting in alkaline solution. *J. Electroanal. Chem.* **2022**, *906*, 116014. [[CrossRef](#)]
55. Anantharaj, S.; Kundu, S.; Noda, S. “The Fe Effect”: A review unveiling the critical roles of Fe in enhancing OER activity of Ni and Co based catalysts. *Nano Energy* **2021**, *80*, 105514. [[CrossRef](#)]
56. Sun, F.; Li, L.; Wang, G.; Lin, Y. Iron incorporation affecting the structure and boosting catalytic activity of β-Co(OH)₂: Exploring the reaction mechanism of ultrathin two-dimensional carbon-free Fe₃O₄-decorated β-Co(OH)₂ nanosheets as efficient oxygen evolution electrocatalysts. *J. Mater. Chem. A* **2017**, *5*, 6849–6859. [[CrossRef](#)]
57. Wang, Y.; He, Y.; Zhou, M. Fabrication of hierarchical Co(OH)₂@Ni(OH)₂ core-shell nanosheets on carbon cloth as an advanced electrocatalyst for oxygen evolution reaction. *Appl. Surf. Sci.* **2019**, *479*, 1270–1276. [[CrossRef](#)]
58. Lei, Y.; Huang, R.; Xie, H.; Zhang, D.; Liu, X.; Si, Y.; Li, N. Electronic structure tuning of FeCo nanoparticles embedded in multi-dimensional carbon matrix for enhanced bifunctional oxygen electrocatalysis. *J. Alloys Compd.* **2021**, *853*, 157070. [[CrossRef](#)]
59. Wu, Y.; Xiao, Z.; Jin, Z.; Li, X.; Chen, Y. The cobalt carbide/bimetallic CoFe phosphide dispersed on carbon nanospheres as advanced bifunctional electrocatalysts for the ORR, OER, and rechargeable Zn-air batteries. *J. Colloid Interface Sci.* **2021**, *590*, 321–329. [[CrossRef](#)]
60. Adamson, W.; Jia, C.; Li, Y.; Zhao, C. Vanadium-induced fragmentation of crystalline CoFe hydr(oxy)oxide electrocatalysts for enhanced oxygen evolution reaction. *Int. J. Hydrog. Energy* **2021**, *46*, 35230–35238. [[CrossRef](#)]
61. Lin, S.-Y.; Chen, Y.-P.; Cao, Y.; Zhang, L.; Feng, J.-J.; Wang, A.-J. Aminouracil-assisted synthesis of CoFe decorated bougainvillea-like N-doped carbon nanoflowers for boosting Zn–air battery and water electrolysis. *J. Power Sources* **2022**, *521*, 230926. [[CrossRef](#)]
62. Lei, Z.; Tan, Y.; Zhang, Z.; Wu, W.; Cheng, N.; Chen, R.; Mu, S.; Sun, X. Defects enriched hollow porous Co-N-doped carbons embedded with ultrafine CoFe/Co nanoparticles as bifunctional oxygen electrocatalyst for rechargeable flexible solid zinc-air batteries. *Nano Res.* **2020**, *14*, 868–878. [[CrossRef](#)]
63. Li, G.; Liu, C.; Zhang, Z.; Cui, B.; Chen, Y.; Deng, Y.; Hu, W. Nano-manufacturing of Co(OH)₂@NC for efficient oxygen evolution/reduction reactions. *J. Mater. Sci. Technol.* **2021**, *81*, 131–138. [[CrossRef](#)]